Analysis of Seismic Signals Generated by Vehicle Traffic with Application to Derivation of Subsurface Q-Values

Haoran Meng[*1], Yehuda Ben-Zion[2,3], and Christopher W. Johnson[4]

Abstract

Correct identification and modeling of anthropogenic sources of ground motion are of considerable importance for many studies, including detection of small earthquakes and imaging seismic properties below the surface. To understand signals generated by common vehicle traffic, we use seismic data recorded by closely spaced geophones normal to roads at two sites on San Jacinto fault zone. To quantify the spatiotemporal and frequency variations of the recorded ground motions, we develop a simple analytical solution accounting for propagation and attenuation of surface waves. The model reproduces well-observed bell-shaped spectrograms of car signals recorded by geophones close to roads, and it can be used to estimate frequency-dependent Q-values of the subsurface materials. The data analysis indicates Q-values of 3–40, for frequencies up to 150 Hz for road-receiver paths at the two examined sites. The derived Q-values are consistent with attenuation factors of surface waves previously obtained with other methods. The analytical results and analysis procedure provide a highly efficient method for deriving Q-values of shallow subsurface materials.

Introduction

Seismic ground motions consist of superposition of contributions from various tectonic (earthquakes and tremor), environmental (e.g., wind shaking objects, lightning, and thunders), and anthropogenic (e.g., car, train, and air traffic) sources (e.g., Seydoux et al., 2016; Meng et al., 2019). Correctly identifying different sources of ground motion is essential for the numerous applications using seismic waveforms, including the detection of small earthquakes and tremor (e.g., Gibbons and Ringdal, 2006; Shelly et al., 2007; Cheng et al., 2020), imaging subsurface structures based on the ambient seismic noise (e.g., Shapiro et al., 2005; Lin et al., 2013; Zigone et al., 2019), and monitoring temporal changes of seismic properties (e.g., Brenguier et al., 2008; Zhan et al., 2013; Hillers et al., 2019).

The San Jacinto fault zone (SJFZ) is a major branch of the North America–Pacific plate boundary in southern California that is highly active seismically and well-instrumented with several regional seismic networks and dense fault-zone arrays (e.g., Hauksson et al., 2012; Ben-Zion et al., 2015; White et al., 2019). The total contribution to the duration of recorded ground motion from tectonic sources, even at this highly active fault zone, is estimated to be around 1% (Meng and Ben-Zion, 2018b). For comparison, air-traffic and wind-related ground motions occupy tens of percent of the seismic waveforms recorded around the SJFZ (Johnson et al., 2019; Meng et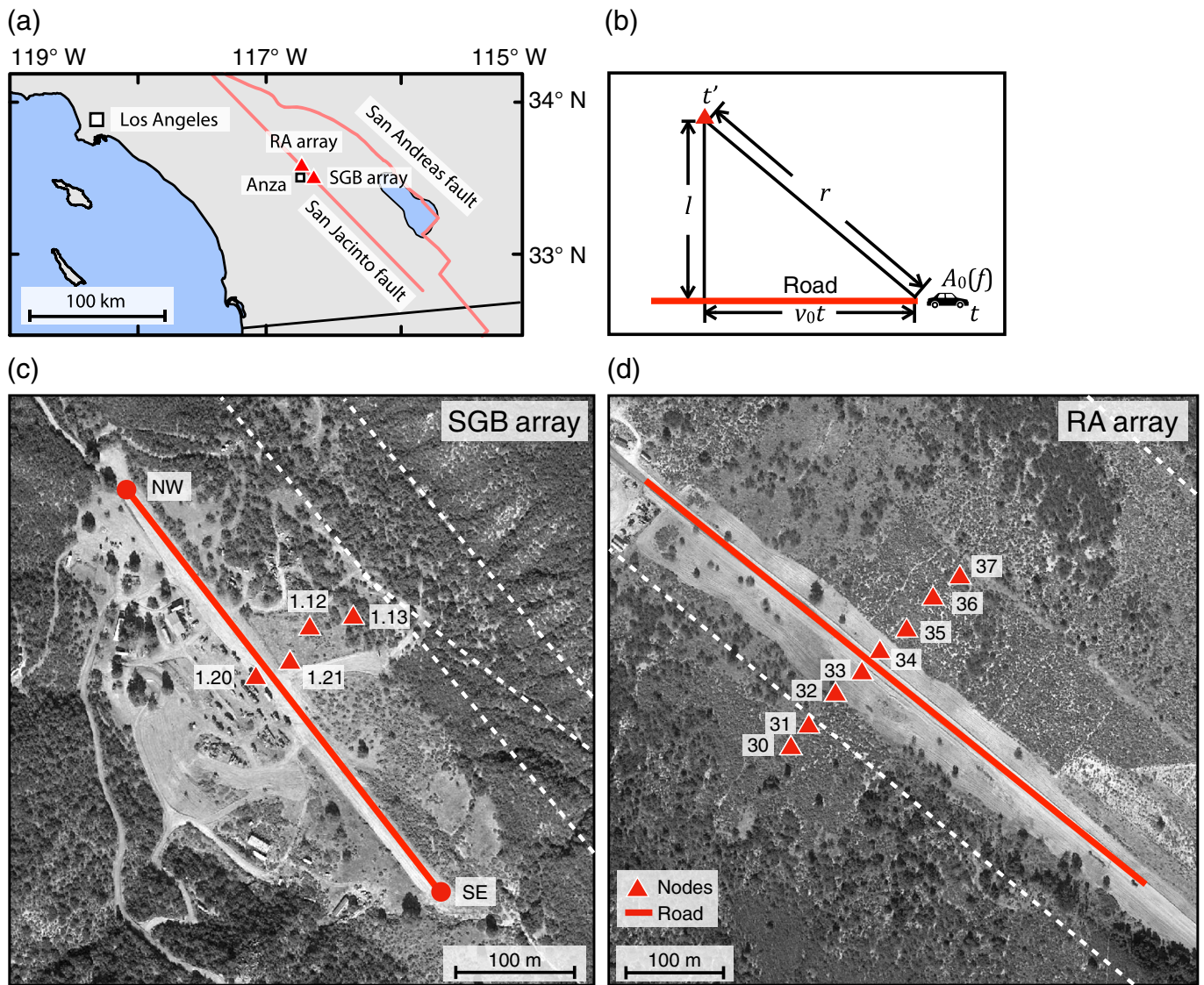 al., 2019). These signals, together with other anthropogenic, sources such as trains and cars, can be nuisances for studies aiming to detect tectonic sources (e.g., Douze and Laster, 1979; Inbal et al., 2018), because they mask tectonic signals and can produce similar bursts and trains of weak ground motions. The correct identification of anthropogenic sources can not only enhance the fidelity of tectonic source detections, but also be utilized for detailed seismic imaging and monitoring changes of properties in the crust (e.g., Nakata et al., 2011; Chang et al., 2016; Brenguier et al., 2019).

Vehicle traffic has been identified in previous studies as a common source contributing to ground motions in continuous seismic waveforms (e.g., Riahi and Gerstoft, 2015; Salvermoser et al., 2015; Lindsey et al., 2020). The focus of this work is to characterize vehicle-induced ground motions, using both controlled and uncontrolled field experiments at sites on the SJFZ. We model car-generated ground motion with analytical expressions that account for the source spectrum and attenuation of Rayleigh waves with increasing propagation distance. The model is constrained using data recorded by two

1. Scripps Institution of Oceanography, University of California, San Diego, San Diego, California, U.S.A.; 2. Department of Earth Sciences, University of Southern California, Los Angeles, California, U.S.A.; 3. Southern California earthquake Center, University of Southern California, Los Angeles, California, U.S.A.; 4. Los Alamos National Laboratory, Los Alamos, New Mexico, U.S.A.

*Corresponding author: h2meng@ucsd.edu

Figure 1. (a) A regional map showing the two seismic arrays (red triangles) on San Jacinto fault zone. (b) A conceptual diagram of a car traveling with constant speed along a straight road. (c, d) Seismic nodes (red triangles) and dirt roads (redlines) shown on a Google Earth image of the Sage Brush Flat (SGB) and Ramona Reservation (RA) sites centered around −116.593°/33.539° and −116.699°/33.607°, respectively. White-dashed lines are mapped U.S. Geological Survey (USGS) fault traces. The color version of this figure is available only in the electronic edition.

deployments of closely spaced seismic sensors aligned orthogonal to roads. Fitting the model results to the data provides a simple tool for deriving frequency-dependent seismic attenuation coefficients for shallow crust materials between the road and sensors.

Seismic Data

The data were recorded by two short (<250 m) linear arrays of 5-Hz Fairfield ZL and seismographs deployed across the Clark branch of the SJFZ at the Sage Brush Flat (SGB) and the Ramona Reservation (RA) sites near Anza California (Fig. 1). At the SGB site, we analyze data recorded at 500 Hz by four sensors with a nominal station spacing of 40 m (Johnson *et al.*, 2018), during a controlled experiment on 6 March 2018 using a mid-size Sport Utility Vehicle (SUV; ~1800 kg) and a compact sedan (~1400 kg). The SGB site is an inactive ranch, with a 500 m hard-packed runway, or dirt road, through the center. The location is relatively isolated from urban noise and was the

subject of numerous previous seismological studies (e.g., Ben-Zion *et al.*, 2015; Hillers *et al.*, 2016; Meng *et al.*, 2019). During the experiment, the vehicles accelerated from one end of the dirt road (red line in Fig. 1c), maintained constant speeds between 10 and 40 km/hr for more than 25 s, and stopped at the other end. The ground motions generated in 14 driving experiments (Table S1, available in the supplemental material to this article) are investigated in this study.

At the RA site, we use data recorded at 500 Hz, by eight sensors with a nominal spacing of 30 m (Allam, 2015), four on each side of a dirt road, during regular (uncontrolled) vehicle traffic with unknown speed (Fig. 1d). The RA site is near the Hog Lake paleoseismic study area, where surface ruptures of over 20 moderate–large events were documented (Rockwell et al., 2015), and was also the subject of previous seismological studies on fault-zone imaging (Yang et al., 2014; Wang et al., 2019; Zigone et al., 2019). The different settings at the two sites allow us to verify that the developed techniques are applicable for a range of conditions.

Modeling and Results
Modeling of vehicle source spectra and wave propagation
To quantitatively analyze the recorded ground motions, we consider a simple model with a car moving at constant velocity v_0 along a straight road. The car is sufficiently far from the sensors and can, therefore, be represented as a point source (Fig. 1b). In the model, the vehicle exerts a downward force on the ground and primarily radiates away from the road Rayleigh waves with a source spectrum $A_0(f)$. The waves generated by the vehicle at time t propagate with a phase velocity $c(f)$ and arrive at the seismograph at time t':

$$t' = t + \frac{r}{c(f)}, \tag{1}$$

in which $r = \sqrt{l^2 + (v_0 t)^2}$ and l is the distance between the receiver and road (Fig. 1b). The vehicle speed v_0 is on the order of 10 m/s (36 km/hr), which is much smaller than the phase velocity of surface waves (>200 m/s) in the frequency range 5–150 Hz. Solving equation (1) for t with $v_0 \ll c(f)$ gives

$$t = t' - \frac{\sqrt{l^2 + (v_0 t')^2}}{c(f)}. \tag{2a}$$

To model data with an arbitrary reference time, we add a reference time t'_0 to equation (2a):

$$t = (t' - t'_0) - \frac{\sqrt{l^2 + [v_0(t' - t'_0)]^2}}{c(f)}. \tag{2b}$$

At $t = 0$, the vehicle is the closest to the seismograph, and the generated ground motion arrives at the seismograph at t'. The arrival time t' can be obtained from the seismograms, for example, at the peak of the vertical ground motions. The reference time can then be determined by

$$t'_0 = t' - \frac{l}{\sqrt{c^2 - v_0^2}}. \tag{3}$$

Assuming that the horizontal force exerted by the vehicle on the ground is negligible compared with the vertical (i.e.,

relatively smooth roads), the radiation pattern is nearly isotropic in all azimuthal directions. Considering the geometrical spreading and attenuation, the recorded amplitude A at frequency f and time t' is given by (e.g., Inbal et al., 2018)

$$A(f, t') = \frac{A_0(f)}{\sqrt{r(t')}} \exp\left(-\pi f \frac{r(t')}{Qc}\right). \tag{4}$$

Taking the natural logarithm of equation (4) gives

$$\ln(A(f, t')) = \ln(A_0(f)) - \frac{1}{4}\ln(l^2 + (v_0 t)^2) - \pi f \frac{\sqrt{l^2 + (v_0 t)^2}}{l} t^*, \tag{5}$$

in which $Q = Q(f)$ is the frequency-dependent quality factor of Rayleigh wave, and $t^*(f) = l/(Q(f)c(f))$ is the attenuation factor that is widely used in seismic attenuation tomography (e.g., Roth et al., 1999; Liu and Zhao, 2015).

The observed spectral amplitude $A(f_i, t'_j)$ for frequency f_i at receiver time t'_j can be obtained by performing Fourier transform on short time windows of recorded waveforms. A computationally convenient form is obtained by rearranging the terms in equation (5) to be

$$\ln(A(f_i, t'_j)) + \frac{1}{4}\ln(l^2 + (v_0 t_j)^2)$$
$$= \begin{bmatrix} 1 & -\pi f_i \frac{\sqrt{l^2 + (v_0 t_j)^2}}{l} \end{bmatrix} \cdot \begin{bmatrix} \ln(A_0(f_i)) \\ t^*(f_i) \end{bmatrix}, \tag{6}$$

in which $t_j = (t'_j - t'_0) - \sqrt{l^2 + [v_0(t'_j - t'_0)]^2}/c(f_i)$. The centered dot in equation (6) represents a dot product and this notation is applied throughout the article. For each frequency, f_i, of interest, measurements of the spectral amplitude $A(f_i, t'_j)$ may be made at multiple time steps. As shown in the Appendix, we can then estimate the source spectrum $\ln(A_0(f_i))$ and the attenuation factor $t^*(f_i)$ from equation (6), using the observations.

Data analysis and results
We first analyze example observations of a controlled vehicle event at the SGB site and a detected vehicle event at the RA site, and then present results for additional vehicle events at both sites. To illustrate the data and analysis procedure, we start by examining the seismic signals generated by a mid-size SUV moving at the SGB site at 40 km/hr and recorded by four sensors with distances from the road of 16, 20, 67, and 110 m (Fig. 1c). The envelopes and amplitudes of the recorded waveforms vary with increasing distance from the road (Fig. 2a). At the two sensors (1.20 and 1.21 in Fig. 1c) near the road, the data have clear central peaks and resemble tremor with a duration of about 20 s. The amplitudes and high-frequency content of the waveforms attenuate rapidly with increasing distances. Spectrograms corresponding to the 25 s waveforms in
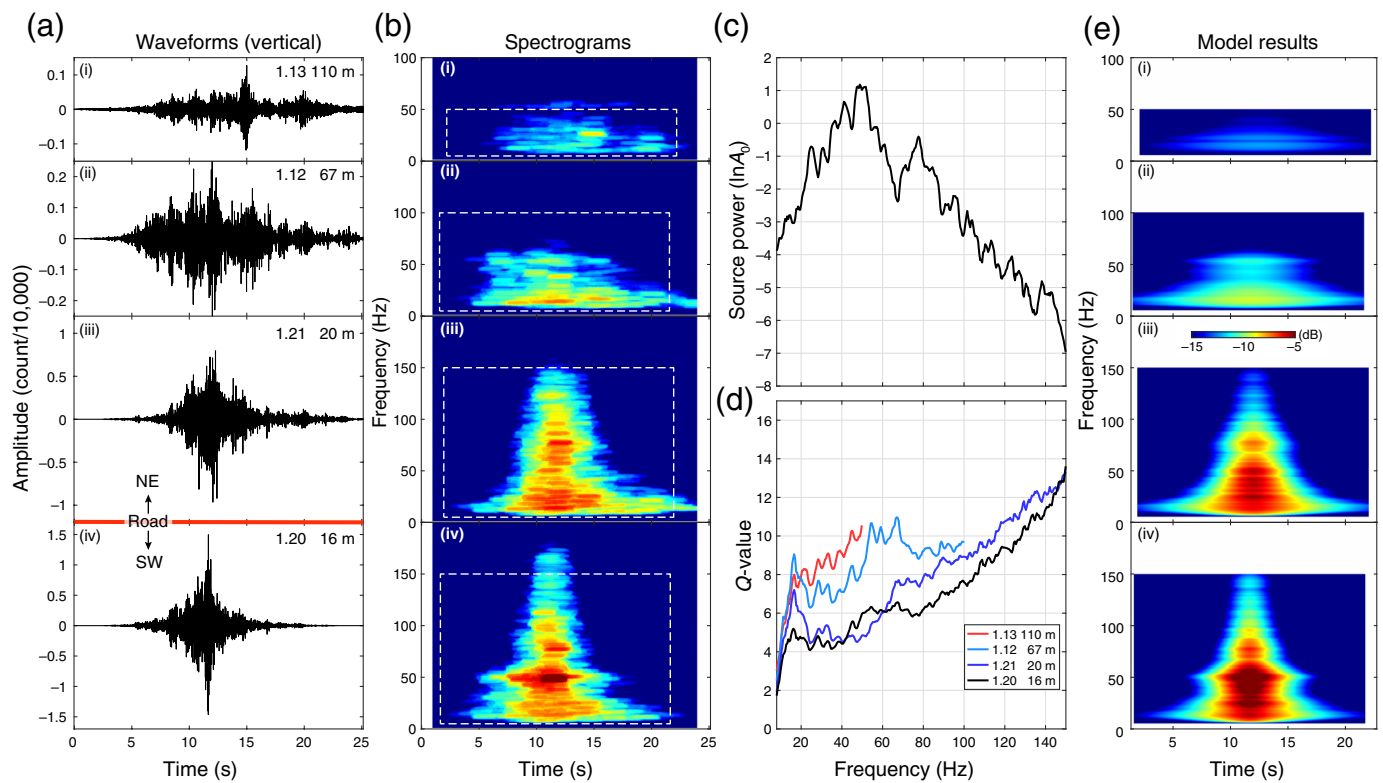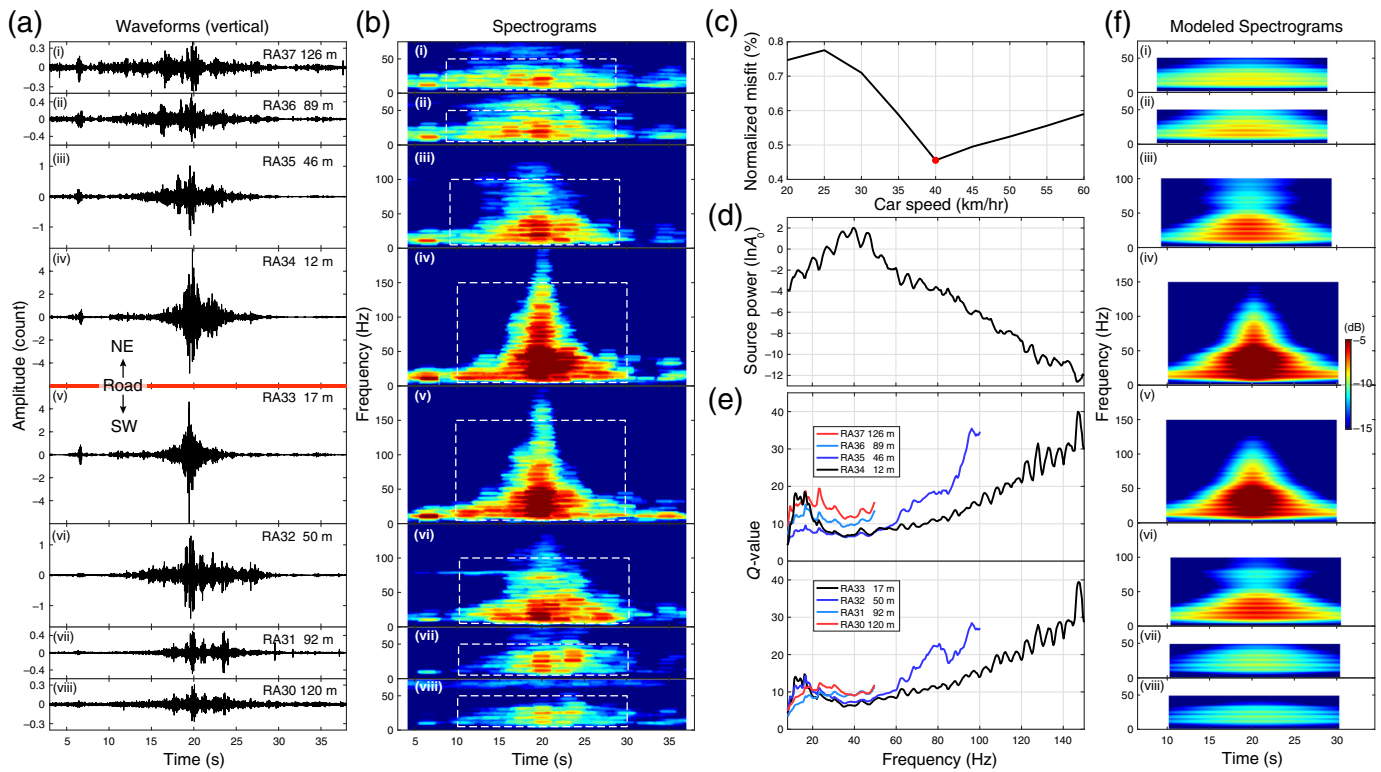
Figure 2. (a) Vertical waveforms recorded by four sensors at the SGB site, during the experiment 1 on 6 March 2018 (Table S1) with a mid-size Sport Utility Vehicle (SUV) moving at 40 km/hr. (b) The corresponding spectrograms with white-dashed boxes denoting data used in the inversion. (c) The resolved source spectrum of the moving car. (d) The derived Q-values between 8 and 150 Hz for paths between the car and sensors. (e) The modeled spectrograms using the resolved source spectrum and Q-values shown in panels (c,d). The color version of this figure is available only in the electronic edition.

Figure 2a are obtained by performing Fourier transform using short moving time intervals of 512 samples (1.024 s) with 256 overlapping samples. The spectrograms have symmetric bell shapes for stations very close to the road (Fig. 2b), and the spectral shapes flatten rapidly with increasing distance. These observations reflect basic aspects of the propagation and attenuation of seismic waves. The data at sensors 1.20 and 1.21 near the road contain signals with high amplitude and frequencies over 150 Hz, when the moving vehicle is in close proximity to the sensors (around 12 s, Fig. 2a,b). Because the vehicle velocity is much less than the seismic wave-propagation speed, the results are, approximately, symmetric when the vehicle is moving toward and away from the sensors (Fig. 2b). At sensors 1.12 and 1.13 located farther from the road at the SGB site (Fig. 1c), similar flattening effects are observed that are due to the higher attenuation and scattering resulting from the larger source-receiver separations (Fig. 2a,b).

As an application of the described methodology, we extract the amplitudes of the spectrograms for 20 s windows highlighted by the white-dashed boxes in Figure 2b recorded in field experiment 1 (Table S1). Using spectral amplitudes for various time and frequency of interest on the spectrograms (Fig. 2b) allows us to stably perform an inversion of the spectrum of a given source and t^* for the paths between the source and multiple receiver locations (see Appendix). In the inversion, the reference time t_0' for each analyzed waveform is determined by the time of the peak ground motion, which varies for each seismograph, with a subtraction of $l/\sqrt{c^2 - v_0^2}$. Because high-frequency waves are attenuated rapidly with growing

propagation distances (Fig. 2b), we estimate Q-values only up to 150, 100, and 50 Hz, as the sensor distances increase from 16 to 110 m. The time windows and frequency bands (dashed boxes in Fig. 2b) that are selected for analysis exceed the noise level in spectral amplitudes. Performing the analysis on data with wider time window or frequency band may result in biased or unstable estimate of Q-values. Figure 2c shows the resolved source spectrum for the mid-size SUV traveling at 40 km/hr during field experiment 1 at the SGB site (Table S1). The source spectrum $\ln(A_0(f_i))$ has a peak at 50 Hz, with decreasing values at lower and higher frequencies. Based on previous seismic imaging results, the average phase velocity $c(f)$ of the shallow material at the SGB site is about 300 m/s (e.g., Hillers *et al.*, 2016; Mordret *et al.*, 2019). For the frequency range of interest (5–150 Hz), the dispersion of surface waves is relatively weak and can be approximated by a constant value, because surface waves with wavelength <60 m only sample the top sedimentary layer and do not
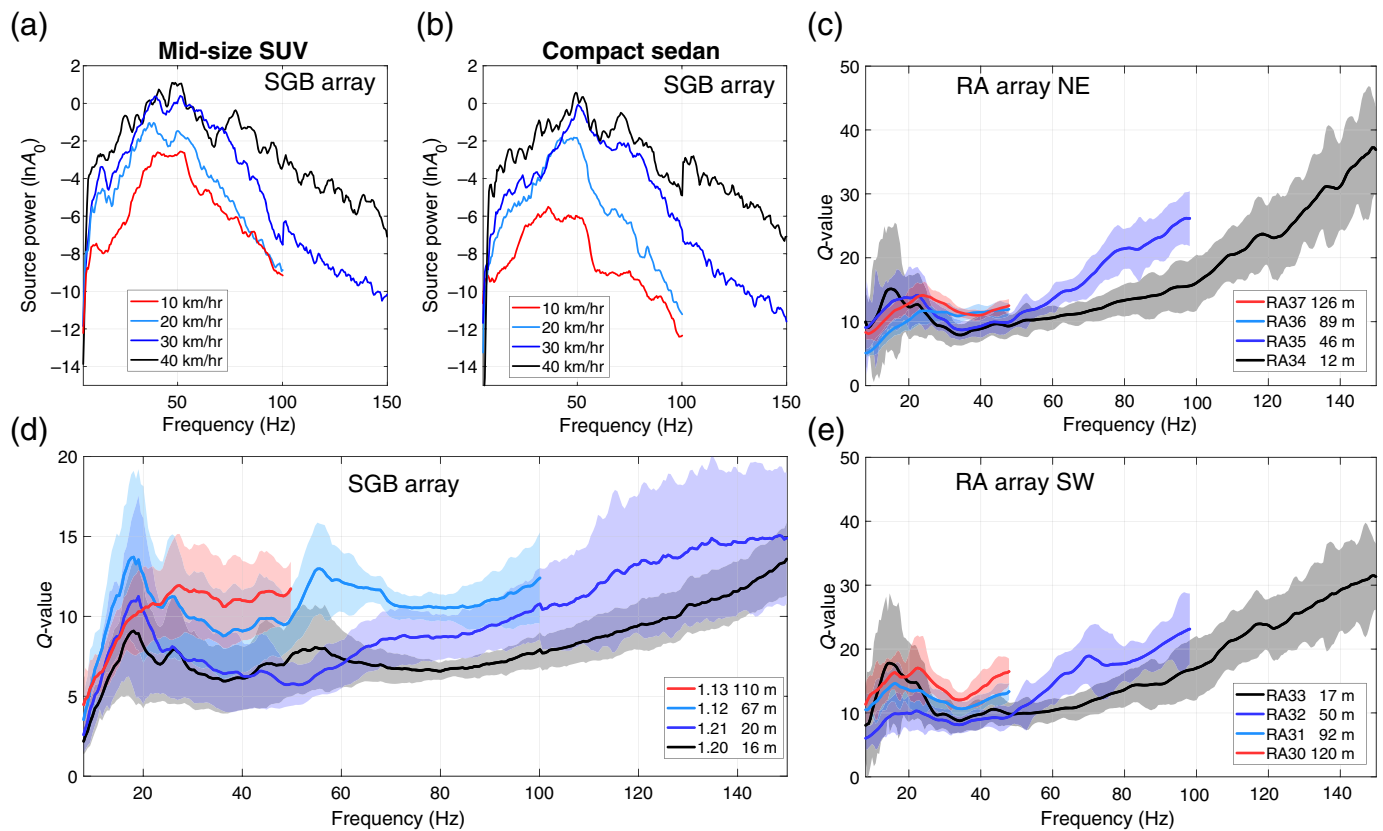
Figure 3. (a) Vertical waveforms recorded by the RA nodal array during the passage of an unknown vehicle (detection 1, Table S2). (b) The corresponding spectrograms with white dashed boxes to denote the data incorporated in the inversion. (c) The gird search results to estimate the vehicle speed with a red dot showing the best fit value. (d) Resolved source spectrum of the moving vehicle. (e) Derived Q-values for paths between the car and sensors. (f) Modeled spectrograms using the resolved vehicle speed, source spectrum, and Q-values in (c,d,e). The color version of this figure is available only in the electronic edition.

interact with the deeper bedrocks (Meng and Ben-Zion, 2018a). Using the relation, $Q(f) = l/(c(f)t^*(f))$ estimate Q-values between 8 and 150 Hz for surface waves propagating in the shallow subsurface materials (<60 m) at the SGB site (Fig. 2d). The estimated Q-values with the same data, representing average quality factors of Rayleigh wave between the road and seismographs, generally increase with frequency and are mostly in the range 4–14 (Fig. 2d). Using equation (5) with the resolved source spectra $\ln(A_0(f_i))$ and Q-values shown in Figure 2c,d, the modeled spectrograms (Fig. 2e) match closely to the observations, given the assumed simplified source spectrum, surface waves propagation, and attenuation (Fig. 2b). The spectrogram modeling provides a consistency check on the analysis procedure and evidence that the source is properly characterized at the level of the recorded data.

To demonstrate the utility of the method for uncontrolled car traffic data, we analyze a detected vehicle event at the RA site (event 1; Table S2) traveling at an unknown speed (Fig. 3). Seismic imaging at the RA site shows that the average Rayleigh-wave phase velocity is about 300 m/s (Zigone *et al.*, 2019). Because v_0 in equation (5) is unknown, a grid search is then performed from 10 to 100 km/hr, using a 5 km/hr increment. The best v_0-value is determined by minimizing the L2 norm of the observed and modeled spectrograms misfit. The estimated speed for the detected vehicle event 1 at the RA site is 40 km/hr (Fig. 3c). The resolved source spectrum has a peak at 40 Hz, and it decreases at lower and higher frequencies (Fig. 3d). Similar to the results at the SGB site, the estimated Q-values at different stations generally increase with

frequencies but span a higher range from 5 to 40 (Fig. 3e). The model spectrograms (Fig. 3f) are consistent with the observed results highlighted by the white boxes in Figure 3b.

To constrain the uncertainties of the estimated Q-values, the inversion is repeated using data recorded during 13 additional field experiments with the mid-size SUV and compact sedan vehicles traveling with known speeds at the SGB site (Table S1), and 10 additional examples of detected vehicle events with unknown speeds at the RA site (Table S2). The resolved source spectra are shown in Figure 4 and Figure S1, and the estimated Q-values for all experiments are presented in Figure 4 as averages and 1 standard deviations. The derived Q-values are consistent with attenuation factors of surface waves obtained from analysis of high-frequency seismic noise in the SJFZ area (Liu *et al.*, 2015) and Q-values of S waves in the upper 50 m, based on shallow logging data in southern California (Fletcher *et al.*, 1990).

(a) Mid-size SUV · SGB array — Source power ($\ln A_0$) vs Frequency (Hz); legend: 10 km/hr, 20 km/hr, 30 km/hr, 40 km/hr

(b) Compact sedan · SGB array — Source power ($\ln A_0$) vs Frequency (Hz); legend: 10 km/hr, 20 km/hr, 30 km/hr, 40 km/hr

(c) RA array NE — Q-value vs Frequency (Hz); legend: RA37 126 m, RA36 89 m, RA35 46 m, RA34 12 m

(d) SGB array — Q-value vs Frequency (Hz); legend: 1.13 110 m, 1.12 67 m, 1.21 20 m, 1.20 16 m

(e) RA array SW — Q-value vs Frequency (Hz); legend: RA33 17 m, RA32 50 m, RA31 92 m, RA30 120 m

Discussion and Conclusions

The vehicle-generated waveforms resemble short-duration tremor near the road, and the corresponding spectrograms have bell shapes, which are indicative of a moving source (Figs. 2 and 3). The amplitudes attenuate rapidly with increasing road-receiver distances, especially for the high frequencies. The sensors at both sites with distances >110 m from the road record signals only at frequencies between 5 and 30 Hz (Figs. 2b and 3b). The source spectra resolved from the vehicle events at SGB and RA sites have, approximately, a triangle shape, with peaks around 40–50 Hz (Fig. 4a,b and Fig. S1). For the field experiments at the SGB site, the source spectra are stronger for the heavier mid-size SUV compared with the compact sedan traveling at the same speed.

The source power generated by both the vehicles is significantly stronger for cars moving at higher speeds, indicating stronger interactions between the vehicles and the road surfaces (Fig. 4a,b). This can be explained by analytical modeling of the vertical forces generated by a vehicle with a given mass, approximated by a single-axle model with a combination of springs and dampers (Hao and Ang, 1998). For a faster-moving vehicle, larger vertical forces are expected to be exerted on the ground surface, as the wheels accelerate and decelerate more rapidly in the vertical direction by rolling over small bumps and the unevenness of the road.

In the developed model, we assume that the vehicle is traveling at constant velocity along a straight road, which is

Figure 4. (a,b) Estimated source spectra of the two experimental vehicles moving at different velocities in the SGB site. (c,e) The resolved average Q-values (solid line) with one standard deviation (shaded area) between the road and sensors at the RA array. (d) The derived Q-values estimated for paths between the road and sensors shown as the average (solid line) with one standard deviation (shaded area). The color version of this figure is available only in the electronic edition.

appropriate for the controlled field experiment at the SGB site. The recorded seismic waveforms and the corresponding spectrogram at the SGB site are relatively symmetric in time (Fig. 2). These features were used as criteria to select the 10 events at the RA site for analysis with the basic developed model (Fig. 3). Vehicles not traveling at a constant speed or moving on a curved road are expected to produce more complex signals (Fig. S3). Modeling these signals becomes more difficult, because the source spectra may change by an unknown speed history and the forces exerted on the road surface evolve during periods of accelerations and decelerations in the vertical and horizontal directions.

We assume that the horizontal force exerted by the vehicle on the ground is negligible compared with the vertical. This is generally true when the vehicle travels at a constant speed on a relatively smooth surface. To test whether this assumption is representative of the conditions relevant for the examined data,
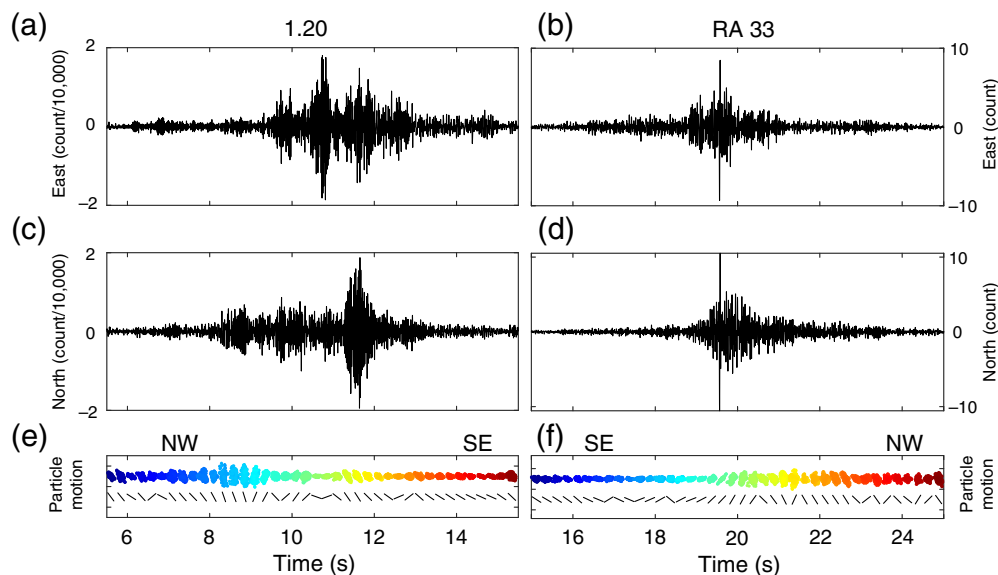
Figure 5. (a,c) Horizontal waveforms recorded by sensor 1.20 at the SGB site, during the experiment 1 on 6 March 2018 (Table S1) with a mid-size SUV moving at 40 km/hr. (b,d) Horizontal waveforms recorded by sensor RA33 at the RA site, during the passage of an unknown vehicle moving at 40 km/hr (detection 1, Table S2). (e) Colored dots show the particle motion for each 0.25 s window (125 samples). Bottom black lines show the fitted particle motion directions for each window. (f) Colored dots show the particle motion for each 0.25 s window (125 samples). Bottom black lines show the fitted particle motion directions for each window. The color version of this figure is available only in the electronic edition.

we analyze the polarizations of the two events discussed in the Data Analysis and Results section (Figs. 2 and 3). Figure 5 shows the horizontal waveforms for experiment 1 (Table S1) at sensor 1.20. We evaluate the horizontal particle motions for each 0.25 s window (125 samples) and then fit directions using a linear-square algorithm. The fitted particle motion directions are initially parallel to the road (6–8 s in Fig. 5e) and then gradually turn clockwise as the vehicle moves toward the sensor. Variations around this pattern are possibly due to unevenness of the road or superposed high-frequency noise generated by wind-related or other sources (Johnson *et al.*, 2019). When the vehicle is closest to the sensor (around 10 s), the particle motion direction is, approximately, perpendicular to the road strike. Because the vehicle moves away from the sensor toward the southwest, the particle motion direction becomes again generally parallel to the road (12–15 s in Fig. 5e). This implies that the moving vehicle primarily exerts a vertical force on the ground, which generates Rayleigh wave with particle motion parallel to the direction from the source to sensor. For detected event 1 (Table S2) at sensor RA33, the horizontal particle motion directions are also generally parallel to the road in the beginning (15–17 s in Fig. 5f) and then turn counterclockwise, implying a moving direction toward the northwest. Because the vehicle moves away from the sensor, the particle motion direction gradually returns to be overall parallel to the road.

The obtained frequency-dependent attenuation coefficients for up to 150 Hz are important results with practical applications, to understanding the properties of the top geotechnical layer (<100 m depth). Simple analytical results and data analysis procedure allow us to easily and stably estimate the source spectra of the moving vehicles and the average *Q*-values between the road and receivers from the data recorded by an array of sensors. Figure 4d summarizes the average and corresponding one standard deviation *Q*-values estimated from the 14 field experiments at the SGB site. The *Q*-values generally increase with frequency and are mostly in the range of 4–14. An increasing trend of frequency-dependent *Q*-values has been widely observed in previous studies (e.g., Aki and Chouet, 1975; Hasegawa, 1985; Mayeda *et al.*, 1992; Erickson *et al.*, 2004). The overall increase of *Q*-values with distances from the road to receivers is consistent with the proximity of the road to the main fault trace and core damage zone at the SGB site (Ben-Zion *et al.*, 2015; Qin *et al.*, 2018; Share *et al.*, 2020). Similar results are found for the *Q*-values estimated from the vehicle traffic events at the RA site, in which the road also follows a main fault trace (Wang *et al.*, 2019; Qin *et al.*, 2020). At this location, the *Q*-values are in the range of 5–40 and again show an increasing trend over growing frequency and distance from the road (Fig. 4c,e). The obtained *Q*-values at both sites are consistent with low-quality factors of surface waves derived from analysis of high-frequency seismic noise in the SJFZ area (Liu *et al.*, 2015) and low *Q*-values of *S* waves in the upper 50 m based on shallow logging data in southern California (Fletcher *et al.*, 1990). Because seismic energy can be trapped in the fault damaged zone (e.g., Ben-Zion and Aki, 1990; Ben-Zion *et al.*, 2003; Hillers *et al.*, 2014), the geometrical decay of the wavefield is expected to be stronger in the fault perpendicular direction than it in the fault parallel direction. Therefore, the resolved increasing trend of *Q*-values with distances from road to receiver at both sites is unlikely caused by an over correction of the geometric spreading factor $1/\sqrt{r}$.

Local peaks in the resolved frequency-dependent *Q*-values are observed around 15–25 Hz at both the sites (Fig. 4c–e).

These peaks are probably produced by the assumed constant phase velocity of Rayleigh waves applied in our analysis. Using a higher phase velocity will reduce the estimated Q-value for an observed attenuation factor $t^*(f) = l/(Q(f)c(f))$. To illustrate this, we introduce a dispersion over the frequency range of 5–25 Hz with a decreasing cosine function of phase velocities from 600 to 300 m/s (Fig. S2a), similar to SJFZ observations (Zigone *et al.*, 2019). Analyzing the data of experiment 1 at the SGB site with the assumed dispersion $c(f)$ reduces the peaks of resolved Q-values around 15–25 Hz (Fig. S2c) while keeping the source spectrum almost unchanged (Fig. S2b). This indicates that the simple modeling procedure described in the Seismic Data section provides stable estimates of the vehicle source spectra and attenuation factor t^*, but the derived Q-values depend, to some extent, on the assumed phase velocities. In addition, the variations of the resolved Q-values at various sensors may be somewhat overestimated for a given frequency, because the phase velocity can also vary across the damage zones (Zigone *et al.*, 2019). Heterogeneities of phase velocities can also perturb the radiation generated by the moving vehicle from the assumed isotropic pattern.

The source spectrum reflecting the interaction between the vehicle and road surface can be represented by a triangle in the frequency domain with a peak at a given frequency, as shown in Figure 4a,b and Figure S1. Using a triangle vehicle source spectrum with a peak at 50 Hz and a constant Q-value of 15 for frequencies 0–150 Hz, we synthesize spectrograms (Fig. S4) that match the observations in Figures 2b and 3b. The modeling results provide guidance to properly identify vehicle traffic events from other sources of weak ground motions commonly observed in continuous seismic records (Inbal *et al.*, 2018; Meng and Ben Zion, 2018b; Johnson *et al.*, 2019, 2020; Meng *et al.*, 2019). By developing a broad model space of source spectra, Q-values, phase velocities, and traveling-speed parameters, we can create a training dataset of spectrogram templates of vehicle events for studies using machine-learning techniques for signal classification. The developed method can also be utilized to monitor temporal variations of attenuation factors of shallow subsurface materials in areas with seismographs deployed near roads. This may be implemented with controlled driving experiments or random vehicle traffic as done at the two different sites in this article.

Data and Resources

The original data used in the study at the Sage Brush Flat (SGB) site and Ramona Reservation (RA) site can be obtained from the International Federation of Digital Seismograph Networks, DOI: 10.7914/SN/7A_2018 (Johnson *et al.*, 2018) and DOI: 10.7914/SN/9K_2015 (Allam, 2015), respectively. The supplemental material for this article includes two tables and four figures.

Conflict of Interest

The authors acknowledge there are no conflicts of interest recorded.

References

Aki, K., and B. Chouet (1975). Origin of coda waves: Source, attenuation, and scattering effects. *J. Geophys. Res.* **80,** no. 23, 3322–3342, doi: 10.1029/JB080i023p03322.

Allam, A. A. (2015). San Jacinto damage zone imaging arrays, International Federation of Digital Seismograph Networks, Dataset/Seismic Network, doi: 10.7914/SN/9K_2015.

Ben-Zion, Y., and K. Aki (1990). Seismic radiation from an *SH* line source in a laterally heterogeneous planar fault zone, *Bull. Seismol. Soc. Am.* **80,** 971–994.

Ben-Zion, Y., Z. Peng, D. Okaya, L. Seeber, J. G. Armbruster, N. Ozer, A. J. Michael, S. Baris, and M. Aktar (2003). A shallow fault-zone structure illuminated by trapped waves in the Karadere–Duzce branch of the North Anatolian fault, western Turkey, *Geophys. J. Int.* **152,** no. 3, 699–717, doi: 10.1046/j.1365-246X.2003.01870.x.

Ben-Zion, Y., F. L. Vernon, Y. Ozakin, D. Zigone, Z. E. Ross, H. Meng, M. White, J. Reyes, D. Hollis, and M. Barklage (2015). Basic data features and results from a spatially dense seismic array on the San Jacinto fault zone, *Geophys. J. Int.* **202,** no. 1, 370–380, doi: 10.1093/gji/ggv142.

Brenguier, F., P. Boué, Y. Ben-Zion, F. Vernon, C. W. Johnson, A. Mordret, O. Coutant, P. E. Share, E. Beaucé, D. Hollis, *et al.* (2019). Train traffic as a powerful noise source for monitoring active faults with seismic interferometry, *Geophys. Res. Lett.* **46,** no. 16, 9529–9536, doi: 10.1029/2019GL083438.

Brenguier, F., N. M. Shapiro, M. Campillo, V. Ferrazzini, Z. Duputel, O. Coutant, and A. Nercessian (2008). Towards forecasting volcanic eruptions using seismic noise, *Nature Geosci.* **1,** no. 2, 126–130, doi: 10.1038/ngeo104.

Chang, J. P., S. A. de Ridder, and B. L Biondi (2016). High-frequency Rayleigh-wave tomography using traffic noise from Long Beach, California, *Geophysics* **81,** no. 2, B43–B53, doi: 10.1190/geo2015-0415.1.

Cheng, Y., Y. Ben-Zion, F. Brenguier, C. W. Johnson, Z. Li, P. E. Share, A. Mordret, P. Boué, and F. Vernon (2020). An automated method for developing a catalog of small earthquakes using data of a dense seismic array and nearby stations, *Seismol. Res. Lett.* **91,** 2862–2871, doi: 10.1785/0220200134.

Douze, E. J., and S. J. Laster (1979). Seismic array noise studies at Roosevelt Hot Springs, Utah geothermal area, *Geophysics* **44,** no. 9, 1570–1583, doi: 10.1190/1.1441027.

Erickson, D., D. E. McNamara, and H. M. Benz (2004). Frequency-dependent *Lg Q* within the continental United States, *Bull. Seismol. Soc. Am.* **94,** no. 5, 1630–1643, doi: 10.1785/012003218.

Fletcher, J. B., T. Fumal, H. P. Liu, and L. C. Carroll (1990). Near-surface velocities and attenuation at two boreholes near Anza, California, from logging data, *Bull. Seismol. Soc. Am.* **80,** no. 4, 807–831.

Gibbons, S. J., and F. Ringdal (2006). The detection of low magnitude seismic events using array-based waveform correlation, *Geophys. J. Int.* **165,** no. 1, 149–166, doi: 10.1111/j.1365-246X.2006.02865.x.

Hao, H., and T. C. Ang (1998). Analytical modeling of traffic-induced ground vibrations, *J. Eng. Mech.* **124,** no. 8, 921–928, doi: 10.1061/(ASCE)0733-9399(1998)124:8(921).

Hasegawa, H. S. (1985). Attenuation of *Lg* waves in the Canadian shield, *Bull. Seismol. Soc. Am.* **75,** no. 6, 1569–1582.

Hauksson, E., W. Yang, and P. M. Shearer (2012). Waveform relocated earthquake catalog for southern California (1981 to June 2011), *Bull. Seismol. Soc. Am.* **102,** no. 5, 2239–2244, doi: 10.1785/0120120010.

Hillers, G., M. Campillo, Y. Ben-Zion, and P. Roux (2014). Seismic fault zone trapped noise, *J. Geophys. Res.* **119,** 5786–5799, doi: 10.1002/2014JB011217.

Hillers, G., M. Campillo, F. Brenguier, L. Moreau, D. C. Agnew, and Y. Ben-Zion (2019). Seismic velocity change patterns along the San Jacinto fault zone following the 2010 M 7.2 El Mayor–Cucapah and M 5.4 Collins Valley earthquakes, *J. Geophys. Res.* **124,** no. 7, 7171–7192, doi: 10.1029/2018JB017143.

Hillers, G., P. Roux, M. Campillo, and Y. Ben-Zion (2016). Focal spot imaging based on zero lag cross-correlation amplitude fields: Application to dense array data at the San Jacinto fault zone, *J. Geophys. Res.* **121,** no. 11, 8048–8067, doi: 10.1002/2016JB013014.

Inbal, A., T. Cristea-Platon, J. P. Ampuero, G. Hillers, D. Agnew, and S. E. Hough (2018). Sources of long-range anthropogenic noise in southern California and implications for tectonic tremor detection sources of long-range anthropogenic noise in southern California, *Bull. Seismol. Soc. Am.* **108,** no. 6, 3511–3527, doi: 10.1785/0120180130.

Johnson, C. W., Y. Ben-Zion, H. Meng, and F. Vernon (2020). Identifying different classes of seismic noise signals using unsupervised learning, *Geophys. Res. Lett.* e2020GL088353, doi: 10.1029/2020GL088353.

Johnson, C. W., H. Meng, F. Vernon, and Y. Ben-Zion (2019). Characteristics of ground motion generated by wind interaction with trees, structures, and other surface obstacles, *J. Geophys. Res.* **124,** no. 8, 8519–8539, doi: 10.1029/2018JB017151.

Johnson, C. W., F. Vernon, N. Nakata, and Y. Ben-Zion (2018). Sage Brush Flats seismic experiment on interaction of wind with ground motion, International Federation of Digital Seismograph Networks, doi: 10.7914/SN/7A_2018.

Lin, F. C., D. Li, R. W. Clayton, and D. Hollis (2013). High-resolution 3D shallow crustal structure in Long Beach, California: Application of ambient noise tomography on a dense seismic array, *Geophysics* **78,** no. 4, Q45–Q56, doi: 10.1190/geo2012-0453.1.

Lindsey, N. J., S. Yuan, A. Lellouch, L. Gualtieri, T. Lecocq, and B. Biondi (2020). City-scale dark fiber DAS measurements of infrastructure use during the COVID-19 pandemic, *Geophys. Res. Lett.* doi: 10.1029/2020gl089931.

Liu, X., Y. Ben-Zion, and D. Zigone (2015). Extracting seismic attenuation coefficients from cross-correlations of ambient noise at linear triplets of stations, *Geophys. J. Int.* **203,** no. 2, 1149–1163, doi: 10.1093/gji/ggv357.

Liu, X., and D. Zhao (2015). Seismic attenuation tomography of the southwest Japan arc: New insight into subduction dynamics, *Geophys. J. Int.* **201,** no. 1, 135–156, doi: 10.1093/gji/ggv007.

Mayeda, K., S. Koyanagi, M. Hoshiba, K. Aki, and Y. Zeng (1992). A comparative study of scattering, intrinsic, and coda Q^{-1} for Hawaii, Long Valley, and central California between 1.5 and 15.0 Hz, *J. Geophys. Res.* **97,** no. B5, 6643–6659, doi: 10.1029/91JB03094.

Meng, H., and Y. Ben-Zion (2018a). Detection of small earthquakes with dense array data: Example from the San Jacinto fault zone, southern California, *Geophys. J. Int.* **212,** no. 1, 442–457, doi: 10.1093/gji/ggx404.

Meng, H., and Y. Ben-Zion (2018b). Characteristics of airplanes and helicopters recorded by a dense seismic array near Anza California, *J. Geophys. Res.* **123,** no. 6, 4783–4797, doi: 10.1029/2017JB015240.

Meng, H., Y. Ben-Zion, and C. W. Johnson (2019). Detection of random noise and anatomy of continuous seismic waveforms in dense array data near Anza California, *Geophys. J. Int.* **219,** no. 3, 1463–1473, doi: 10.1093/gji/ggz349.

Mordret, A., P. Roux, P. Boué, and Y. Ben-Zion (2019). Shallow three-dimensional structure of the San Jacinto fault zone revealed from ambient noise imaging with a dense seismic array, *Geophys. J. Int.* **216,** no. 2, 896–905, doi: 10.1093/gji/ggy464.

Nakata, N., R. Snieder, T. Tsuji, K. Larner, and T. Matsuoka (2011). Shear wave imaging from traffic noise using seismic interferometry by cross-coherence, *Geophysics* **76,** no. 6, SA97–SA106, doi: 10.1190/geo2010-0188.1.

Qin, L., Y. Ben-Zion, H. Qiu, P. E. Share, Z. E. Ross, and F. L. Vernon (2018). Internal structure of the San Jacinto fault zone in the trifurcation area southeast of Anza, California, from data of dense seismic arrays, *Geophys. J. Int.* **213,** no. 1, 98–114, doi: 10.1093/gji/ggx540.

Qin, L., P. E. Share, H. Qiu, A. A. Allam, F. L. Vernon, and Y. Ben-Zion (2020). Internal structure of the San Jacinto fault zone at the Ramona Reservation, north of Anza, California, from dense array seismic data, *Geophys. J. Int.* **224,** no. 2, 1225–1241, doi: 10.1093/gji/ggaa482.

Riahi, N., and P. Gerstoft (2015). The seismic traffic footprint: Tracking trains, aircraft, and cars seismically, *Geophys. Res. Lett.* **42,** no. 8, 2674–2681, doi: 10.1002/2015GL063558.

Rockwell, T. K., T. E. Dawson, J. Y. Ben-Horin, and G. Seitz (2015). A 21-event, 4,000-year history of surface ruptures in the Anza seismic gap, San Jacinto fault, and implications for long-term earthquake production on a major plate boundary fault, *Pure Appl. Geophys.* **172,** no. 5, 1143–1165, doi: 10.1007/s00024-014-0955-z.

Roth, E. G., D. A. Wiens, L. M. Dorman, J. Hildebrand, and S. C. Webb (1999). Seismic attenuation tomography of the Tonga–Fiji region using phase pair methods, *J. Geophys. Res.* **104,** no. B3, 4795–4809, doi: 10.1029/1998JB900052.

Salvermoser, J., C. Hadziioannou, and S. C. Stahler (2015). Structural monitoring of a highway bridge using passive noise recordings from street traffic, *J. Acoust. Soc. Am.* **138,** 3864–3872, doi: 10.1121/1.4937765.

Seydoux, L., N. M. Shapiro, J. de Rosny, F. Brenguier, and M. Landès (2016). Detecting seismic activity with a covariance matrix analysis of data recorded on seismic arrays, *Geophys. J. Int.* **204,** no. 3, 1430–1442, doi: 10.1093/gji/ggv531.

Shapiro, N. M., M. Campillo, L. Stehly, and M. H. Ritzwoller (2005). High resolution surface-wave tomography from ambient seismic noise, *Science* **29,** 1615–1617, doi: 10.1126/science.1108339.

Share, P. E., P. Tábořík, P. Štěpančíková, J. Stemberk, T. K. Rockwell, A. Wade, J. R. Arrowsmith, A. Donnellan, F. L. Vernon, and Y. Ben-Zion (2020). Characterizing the uppermost 100 m structure of the San Jacinto fault zone southeast of Anza, California, through joint analysis of geological, topographic, seismic and resistivity data, *Geophys. J. Int.* **222,** no. 2, 781–794, doi: 10.1093/gji/ggaa204.

Shelly, D. R., G. C. Beroza, and S. Ide (2007). Non-volcanic tremor and low-frequency earthquake swarms, *Nature* **446,** no. 7133, 305–307, doi: 10.1038/nature05666.

Wang, Y., A. A. Allam, and C. Lin (2019). Imaging the fault damage zone of the San Jacinto fault near Anza with ambient noise tomography using a dense nodal array, *Geophys. Res. Lett.* **46,** 12,938–12,948, doi: 10.1029/2019GL084835.

White, M. C., Y. Ben-Zion, and F. L. Vernon (2019). A detailed earthquake catalog for the San Jacinto fault-zone region in southern California, *J. Geophys. Res.* **124,** no. 7, 6908–6930, doi: 10.1029/2019JB017641.

Yang, H., Z. Li, Z. Peng, Y. Ben-Zion, and F. Vernon (2014). Low-velocity zones along the San Jacinto fault, southern California, from body waves recorded in dense linear arrays, *J. Geophys. Res.* **119,** no. 12, 8976–8990.

Zhan, Z., V. C. Tsai, and R. W. Clayton (2013). Spurious velocity changes caused by temporal variations in ambient noise frequency content, *Geophys. J. Int.* **194,** 1574–1581, doi: 10.1093/gji/ggt170.

Zigone, D., Y. Ben-Zion, M. Lehujeur, M. Campillo, G. Hillers, and F. L. Vernon (2019). Imaging subsurface structures in the San Jacinto fault zone with high-frequency noise recorded by dense linear arrays, *Geophys. J. Int.* **217,** no. 2, 879–893, doi: 10.1093/gji/ggz069.

Appendix

In the Appendix, we show the implementation of the inversion for a vehicle traffic event recorded at multiple sensors. Assuming there are in total N sensors, the distance between road and sensor k is l_k. The surface wave generated by the vehicle at time t_j propagates with a phase velocity $c(f_i)$ and arrives at the sensor k at time t_j'. The observed spectral amplitude $A_k(f_i, t_j')$ for frequency f_i at receiver time t_j' can be obtained by performing Fourier transform on short windows of recorded waveforms. Here, we let

$$b_k(f_i, t_j') = \ln(A_k(f_i, t_j')) + \frac{1}{4}\ln(l_k^2 + (v_0 t_j)^2), \tag{A1}$$

and

$$a_k(f_i, t_j') = -\pi f_i \frac{\sqrt{l_k^2 + (v_0 t_j)^2}}{l_k^2}, \tag{A2}$$

in which $t_j = (t_j' - t_0') - \sqrt{l_k^2 + [v_0(t_j' - t_0')]^2}/c(f_i)$ and t_0' varies with sensors. Equation (6) can then be simplified as

$$b_k(f_i, t_j') = [\,1 \quad a_k(f_i, t_j')\,] \cdot \begin{bmatrix} \ln(A_0(f_i)) \\ t_k^*(f_i) \end{bmatrix}, \tag{A3}$$

in which $A_0(f_i)$ is the source spectrum and $t_k^*(f_i) = \frac{l_k}{Q_k(f)c(f)}$. Considering one event for N sensors sharing identical source spectrum, equation (A3) can be expanded as

$$\begin{bmatrix} b^1(f_i, t_j') \\ b^2(f_i, t_j') \\ \vdots \\ b^k(f_i, t_j') \\ \vdots \\ b^N(f_i, t_j') \end{bmatrix} = [1^{N\times1}\ A(f_i, t_j')^{N\times N}] \cdot \begin{bmatrix} \ln(A_0(f_i)) \\ t_1^*(f_i) \\ t_2^*(f_i) \\ \vdots \\ t_k^*(f_i) \\ \vdots \\ t_N^*(f_i) \end{bmatrix}, \tag{A4}$$

in which $A(f_i, t_j')^{N\times N} = \mathrm{diag}(a_1(f_i, t_j'), a_2(f_i, t_j'), \ldots, a_k(f_i, t_j'), \ldots, a_N(f_i, t_j'))$. For a given frequency f_i, each measurement at time t_j' can build a linear system using equation (A3). By padding the measurements made at various time steps, we can stably estimate $\ln(A_0(f_i))$ and $t_k^*(f_i)$ by performing an inversion of the overdetermined linear system. Repeating this procedure for all frequencies of interests gives the source spectra and frequency-dependent Q-values at all analyzed sensors. It is also possible to perform the inversion for all frequencies of interest at once and apply a regularization term, such as Laplacian smoothing, to stabilize the results.